Pressure-induced superconductivity in the $RhBi_2$ polymorphs

KeYuan Ma,[1,*] Lifen Shi,[1] Samuel Gallego Parra,[2,3] Oksana E. Kvitnitskaya,[4,5] Dmitri Efremov,[4] Jonathan Noky,[1] Qing Dong,[6] Walter Schnelle,[1] Yurii Prots,[1] Thomas Doert,[7] Helge Rosner,[1] Claudia Felser,[1] and Sergey A. Medvedev[1,†]

[1]*Max Planck Institute for Chemical Physics of Solids, Nöthnitzer Straße 40, 01187 Dresden, Germany*

[2]*Instituto de Diseño para la Fabricacióny Producción Automatizada, MALTA Consolider Team, Universitat Politècnica de València, 46022 Valencia, Spain*

[3]*European Synchrotron Radiation Facility (ESRF), 38043 Grenoble, France*

[4]*Leibniz-Institute for Solid State and Materials Research (IFW), 01069 Dresden, Germany*

[5]*B. Verkin Institute for Low Temperature Physics and Engineering of the National Academy of Sciences of Ukraine, 61103 Kharkiv, Ukraine*

[6]*State Key Laboratory of High Pressure and Superhard Materials, Jilin University, Changchun 130012, China*

[7]*TUD Dresden University of Technology, 01062 Dresden, Germany*

(Received 28 January 2026; revised 23 June 2026; accepted 24 September 2026; published 3 November 2026)

The polymorphic rhodium-bismuth compound $RhBi_2$ has attracted interest owing to its nontrivial topological electronic states. We report the growth of single crystals of both α- and β-$RhBi_2$ and a study of their physical properties at low temperatures and ambient and high pressures beyond 40 GPa. At ambient pressure, β-$RhBi_2$ is a metal with a low density of states at the Fermi level, whereas α-$RhBi_2$ is a semimetal with large magnetoresistance (∼500%). Point-contact Andreev-reflection spectroscopy demonstrates induced superconductivity for both phases. By applying pressure, we observe the emergence of superconductivity at $p \approx 8$ GPa in β-$RhBi_2$ and at $p \approx 20$ GPa in α-$RhBi_2$, with the critical temperature T_c exhibiting a dome-shaped dependence on pressure in both phases. The maximum values of T_c are 6.6 K at $p \approx 13$ GPa for β-$RhBi_2$ and 3.7 K at $p \approx 24.2$ GPa for α-$RhBi_2$. Synchrotron x-ray diffraction studies show that the crystal structure of α-$RhBi_2$ remains stable over the entire investigated pressure range. In contrast, β-$RhBi_2$ undergoes a transition from a triclinic to a tetragonal structure (γ-$RhBi_2$) at $p \approx 13.5$ GPa, accompanied by the attainment of the maximum value of T_c.

DOI: 10.1103/8bx1-db7f

I. INTRODUCTION

Intermetallic compounds—compounds of two or more metals with defined composition and crystal structures—have attracted considerable attention for a long time as advanced materials [1]. Group 15 metals (Sb, Bi) are interesting starting elements for the preparation of intermetallic compounds with potential unusual physical properties owing to their versatile crystal chemistry at ambient as well as nonambient conditions [2]. For several of these compounds, unusual topological electronic properties have been reported [3–6], thus highlighting the need to study the interplay between the topological states, transport, and other physical properties of materials.

Superconductivity (sc) and topology are two intriguing phenomena of quantum condensed phases. The former arises owing to electron pairing; the latter emerges from the crystal and atomic orbital symmetries. Among these materials discussed above, various Bi-containing topological insulators have been found to be intrinsic superconductors, either by applying chemical pressure or doping [7–9] or by applying external pressure [10,11]. However, the origin of superconductivity in these materials remains elusive, varying from one material to another [12,13]. For example, superconductivity in the topological insulators YPtBi [14,15], LuPtBi [16], LuPdBi [17], and HoPdBi [18] occurs at ambient pressure and extends beyond the conventional spin-triplet pairing mechanism [19]. The emergence of superconductivity in these materials establishes a connection between superconductivity and topological states and suggests the potential for the realization of unconventional superconductivity.

The binary Rh–Bi phase diagram has been a subject of study over several decades [20–23], also due to interest in superconductivity [21,22]. It contains the stoichiometric compounds RhBi, $RhBi_2$, $RhBi_3$, $RhBi_4$ [21–23], and metastable Rh_3Bi_{14} [2,22–24]. RhBi, $RhBi_4$, and Rh_3Bi_{14} reveal superconductivity below critical temperatures T_c of 2.06, 2.82, and 3.15 K, respectively [21,22,24].

$RhBi_2$ is a polymorphic system that exhibits two distinct phases, whose crystal structures depend on the growth conditions [21–23]. High-temperature β-$RhBi_2$ has a triclinic structure of space group $P\bar{1}$ constituted by layers of condensed polyhedral around Rh atoms stacked along the crystallographic a axis [25], with van der Waals interaction between the layers [Fig. 1(a)]. In this structure, each Rh atom is coordinated by seven Bi species. Rh atoms are located in the center of the polyhedron spanned by a triangle and a square

*Contact author: keyuan.ma@cpfs.mpg.de
†Contact author: Sergiy.Medvediev@cpfs.mpg.de

Published by the American Physical Society under the terms of the Creative Commons Attribution 4.0 International license. Further distribution of this work must maintain attribution to the author(s) and the published article's title, journal citation, and DOI. Open access publication funded by Max Planck Society.

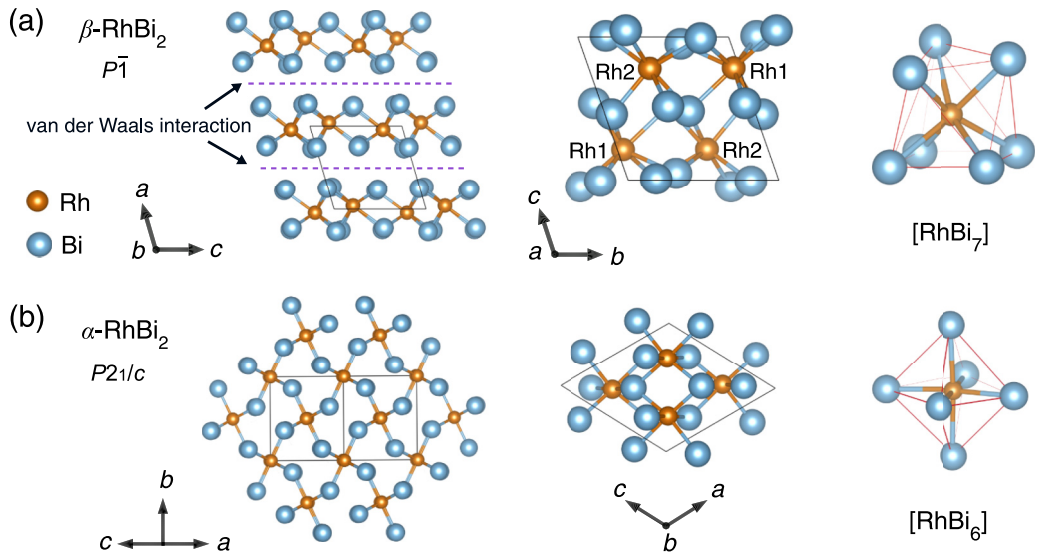


FIG. 1. Crystal structures of the two $RhBi_2$ polymorphs viewed along different directions and Rh atom coordination polyhedra: (a) β-$RhBi_2$ and (b) α-$RhBi_2$.

arranged nearly parallel [Fig. 1(a)]. This coordination can be referred to as a "tetragonal base-trigonal base" type according to the classification by Muetterties and Wright [26]. Upon slow cooling, it transforms to the α-$RhBi_2$ phase, which is stable at room temperature and crystallizes in the monoclinic space group $P2_1/c$. In this phase, the Rh atoms are octahedrally coordinated [Fig. 1(b)], and the structure resembles a slightly distorted monoclinic variant of the marcasite-type structure [25]. β-$RhBi_2$ can be stabilized by fast quenching. The reversible first-order structural phase transition between the α and β phases occurs at $T \approx 430\,^{\circ}$C [21–23].

Both polymorphs of $RhBi_2$ are reportedly metallic and nonsuperconducting at ambient pressure and temperatures above 1.8 K [21,22,27]. Very recently, triclinic β-$RhBi_2$ has been demonstrated to possess weak topological insulator properties with a van Hove singularity point close to the Fermi energy E_F. Thus one may tune the electronic structure by subjecting the crystals to pressure or strain and possibly discover intriguing new phenomena [27]. First-principles calculations of the electronic band structure of monoclinic α-$RhBi_2$ revealed topological surface states on the (100) surface near E_F, proposing a potential platform for topological superconductivity [28]. However, in these calculations, α-$RhBi_2$ was erroneously considered as a superconductor at ambient pressure [28], although experimentally observed superconducting transitions in samples intended to be $RhBi_2$ have been explained by the presence of superconducting RhBi and $RhBi_4$ phases in the specimens [21]. While α-$RhBi_2$ does not become superconducting at ambient pressure, the application of pressure and strains can result in band inversion and/or an increase in the electronic density of states near E_F, eventually leading to superconductivity [28].

Pressure application is a powerful tool for the controlled tuning of interatomic distances, and, consequently, the properties of the investigated system. In response to the application of high pressure, condensed matter undergoes structural, electronic, magnetic, and other phase transitions [29]. Pressure is very useful to explore new superconducting phases in compounds that are nonsuperconducting at ambient pressure. As such, it is an excellent tool for obtaining insights into the interplay between crystal structure and the peculiarities of the electronic band structure and superconductivity.

Here, we present a study of the physical properties of the two $RhBi_2$ polymorphs at ambient and high pressures. At ambient pressure, the electronic transport, magnetic susceptibility, specific heat capacity, and point-contact Andreev-reflection spectra were measured on single crystals. The effect of pressure on the electronic transport properties and crystal structures was investigated at quasi-hydrostatic pressures up to 45 GPa. We demonstrate that both $RhBi_2$ phases exhibit pressure-induced superconductivity with a dome-shaped dependence of the critical temperature on pressure.

II. EXPERIMENTAL DETAILS

Single crystals of β-$RhBi_2$ were grown using excess Bi as flux, as reported previously [27]. Rhodium powder (99.95%, Alfa Aesar) and bismuth pieces (99.9999%, chemPUR) were mixed at a molar ratio of 1:4 and loaded into an alumina crucible with a filter in the middle. The crucible was sealed in a quartz tube under vacuum, heated up to 900 °C over 4 h, and held for 10 hours. Then, it was slowly cooled down to 520 °C for 200 hours and kept at this temperature for 48 hours. Finally, the excess Bi was separated from the crystals using a centrifuge at 520 °C and quenched in cold water. The resulting crystals were very soft and could be easily exfoliated to obtain a freshly exposed crystal surface (Supplemental Material, Fig. S1) [30].

Crystalline α-$RhBi_2$ samples were obtained by annealing single crystals of the β-$RhBi_2$ modification in a vacuum-sealed quartz tube at a very slow cooling rate. The tube was heated to 480 °C for 10 h, held at this temperature for 12 h, and progressively cooled to room temperature within 21 days. Unlike β-$RhBi_2$ crystal, α-$RhBi_2$ crystals are very brittle and cannot be exfoliated into thin flakes.

Scanning electron microscopy coupled with energy-dispersive x-ray spectroscopy (EDX) was used to evaluate the composition of the grown $RhBi_2$ crystals. The crystal structure and the phase purity of the grown crystals were checked using laboratory single-crystal x-ray diffraction (SCXRD) measurements.

The crystal structure of $RhBi_2$ polymorphs was re-examined by combining laboratory SCXRD and synchrotron powder x-ray diffraction (PXRD) techniques. The specimens used for SCXRD were mechanically extracted from the grown crystal. Owing to strong absorption, the size of an irregularly shaped block was limited to ∼30 μm, and Ag radiation (absorption coefficient $\mu = 69.1\ \mathrm{mm}^{-1}$) was selected. Data collection was performed using a Rigaku XtaLAB Synergy diffraction system equipped with a microfocus sealed x-ray tube and a photon-counting Eiger2 1M detector. PXRD was performed using a high-resolution synchrotron source (ID22 beamline at ESRF). A small part of the grown crystal in the α phase was pulverized to less than 32 μm and loaded into a glass capillary. The preparation of a high-quality powder of the β-phase was hindered by the deformation of this soft material during the attempt to pulverize it. We overcame this problem by preparing β-phase powder by annealing α-modification powder at 560 °C for two weeks, followed by subsequent quenching in water. Data acquisition was performed in Debye–Scherrer geometry using a 13-crystal multianalyzer stage [31]. Lattice parameters were determined by extracting the individual peak positions by profile fitting using LaB_6 as an internal standard (WINCSD software package) [32].

For the point-contact (PC) Andreev-reflection spectroscopy, PCs of the pressure type were created directly in a cryostat by mechanically touching a thin wire (diameter 0.1 mm) of elemental metals (Cu, Ag, Pt, and Ni) onto the surface of the crystals. We measured current-voltage $I(V)$ and the differential resistance $[dV/dI(V)]$ characteristics of the PCs by sweeping the DC current I, on which a small AC current I was superimposed, and detecting the first harmonic of the AC signal using a standard lock-in technique in a four-probe configuration. The measurements were performed directly in the 1.5–10 K temperature range and in a magnetic field up to 10 T. Point contacts with a ferromagnetic Ni counterelectrode were unstable in a magnetic field. For $RhBi_2$-Ni PCs only temperature measurements were performed for both phases.

For high-pressure electrical transport studies, a diamond anvil cell with 500 μm culets was used. The tungsten gasket was insulated against electrical leads with a cubic BN/epoxy mixture. A single-crystal sample of a near-square shape with ∼120 μm in size and ∼10 μm thick was loaded into the sample chamber (diameter 200 μm and height 40 μm) filled with NaCl as a pressure-transmitting medium. Four electrical leads, fabricated from 5-μm-thick Pt foil, were contacted to the surface of the sample in van der Pauw configuration. The electrical resistivity was measured at different pressures using the ETO option of a Quantum Design PPMS using low-frequency AC excitation at temperatures down to 1.8 K and in a magnetic field up to 9 T. All measurements were performed in out-of-plane geometry, with the magnetic field perpendicular to the sample plane.

High-pressure synchrotron XRD structural studies were performed at the P02.2 Extreme Conditions Beamline at Deutsche Elektronen Synchrotron (DESY), Hamburg [33]. A 0.2904 Å wavelength was employed, with a beam size of 2 × 2 μm^2, and a PerkinElmer XRD1621 flat-panel area detector was used. The $RhBi_2$ samples were loaded in a membrane-type diamond anvil cell in a rhenium gasket with neon gas as the pressure-transmitting medium. The pressure was determined using the ruby luminescence method. The pressure dependence of the structure of α-$RhBi_2$ was investigated using PXRD, while for β-$RhBi_2$, the SCXRD technique was used. The PXRD patterns of α-$RhBi_2$ obtained were processed and analyzed using Dyoptas [34] and the GSAS-II software package [35]. CeO_2 was used to calibrate the instrumental model for PXRD acquisition. The CrysAlisPro (version 1.171.43.105a) program suite [36] was used for SCXRD data reduction. The crystal structures were solved using the dual-space algorithm provided by the SHELXT program [37] and then refined using the full-matrix least-squares via the SHELXL program [38]. Both codes are included in the OLEX2 (v1.5) program suite [39]. Enstatite (MgSiO3) was used to calibrate the instrumental model for SCXRD acquisition. VESTA [40] was used to visualize the crystal structures.

We studied the electronic structure by performing full-relativistic density functional theory (DFT) calculations using the full-potential local-orbital FPLO package [41]. We used the generalized gradient approximation (GGA) for the exchange-correlation term. A k-mesh of $12 \times 12 \times 12k$ points in the whole Brillouin zone was employed. Calculations were performed using the experimental crystal structure as input. Under applied pressure, the atomic positions were obtained by relaxing the internal coordinates (at fixed lattice parameters) [42]. The PHONOPY package [43] was employed together with VASP software [44] on a 2 × 2 × 2 supercell for the phonon spectrum calculations of α-$RhBi_2$.

III. RESULTS AND DISCUSSION

A. Ambient pressure characterization

1. Structural refinement

The refinement of the laboratory SCXRD pattern of α-$RhBi_2$, with the structural model in the monoclinic space group $P2_1/c$ with one Rh and two Bi positions, showed a strong tendency to twinning. The latter was expected considering the structural peculiarities of α-$RhBi_2$, e.g., the pseudohexagonal metric of the unit cell and, particularly, the pseudohexagonal subcell of the Rh atoms. The implementation of the twin matrix [001, 0$\bar{1}$0, 100] drastically reduces the residuals from $R_1 = 0.175$ and $wR_2 = 0.405$ to $R_1 = 0.019$ and $wR_2 = 0.039$. Owing to twinning, the determined lattice parameters were deemed insufficiently precise. As such, PXRD was performed using a high-resolution synchrotron source. The resulting pattern showed a clear separation of the corresponding diffraction peaks, e.g., (200) and (002), which allows correct indexing (Fig. 2). The obtained lattice parameters [$a = 6.92185(4)$ Å, $b = 6.79472(8)$ Å, $c = 6.96244(4)$ Å, and $\beta = 117.733(1)°$] were used in the final runs of the refinement of the SCXRD data. All atoms in the structure of α-$RhBi_2$ are located on the general

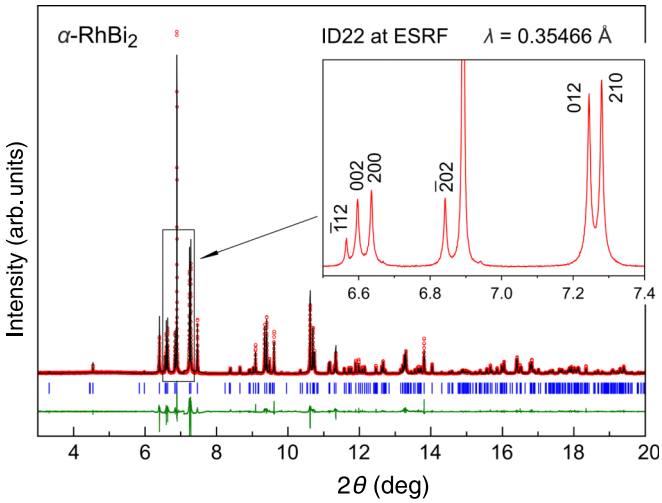


FIG. 2. High-resolution PXRD pattern of α-$RhBi_2$(space group $P2_1/c$). The red dots indicate the experimental points; the black solid line shows the calculated pattern; the blue ticks are the peak positions; and the green line indicates the difference between the measured and calculated intensities. The inset shows a selected area of the experimental diagram, demonstrating a separation of the reflections 200 and 002 and 012 and 210, which clearly indicate different lattice parameters a and c.

sites 4e of space group $P2_1/c$ with refined atomic coordinates Rh(0.22808(6) 0.00201(8) 0.21478(7)), Bi1 (0.15435(4) 0.64137(3) 0.32785(5)), and Bi2 (0.35322(4) 0.35945(3) 0.12955(5)).

The refinement of the laboratory SCXRD pattern of β-$RhBi_2$ was also complicated by stacking faults (as frequently observed in layered structures), which are generated inevitably during the quenching of the sample. Furthermore, the β phase is also prone to forming twins [25]. Synchrotron PXRD was performed for the structural characterization of the β-$RhBi_2$ samples. The obtained PXRD pattern (Supplemental Material, Fig. S2 [30]) exhibits sharp, well-resolved reflections that can be unambiguously assigned to the triclinic $P\bar{1}$ structure of β-$RhBi_2$. The structural parameters of the β-$RhBi_2$ obtained from the refinement of the synchrotron PXRD data were used to further analyze the SCXRD patterns.

The refined structural parameters of both $RhBi_2$ polymorphs are summarized in Table S1 [30].

2. *Physical properties of α- and β-RhBi₂*

The temperature-dependent resistivity $\rho(T)$ for both α- and β-$RhBi_2$ [Fig. 3(a)] shows clearly metallic behavior without any discontinuity owing to phase transitions down to 1.8 K. The residual resistivity ratios (RRR), $\rho(300K)/\rho(1.8K)$, were determined to be 12 and 8.3 for the α- and β-$RhBi_2$ crystals, respectively, with the latter being similar to that in a previous study ($\approx$6) [27].

The magnetic susceptibility as a function of temperature $\chi(T)$ for α- and β-$RhBi_2$ reveals a diamagnetic response with nearly temperature-independent behavior, with a small and negative value of χ over the entire temperature range [Fig. 3(b)], in agreement with previous studies [27,45]. This

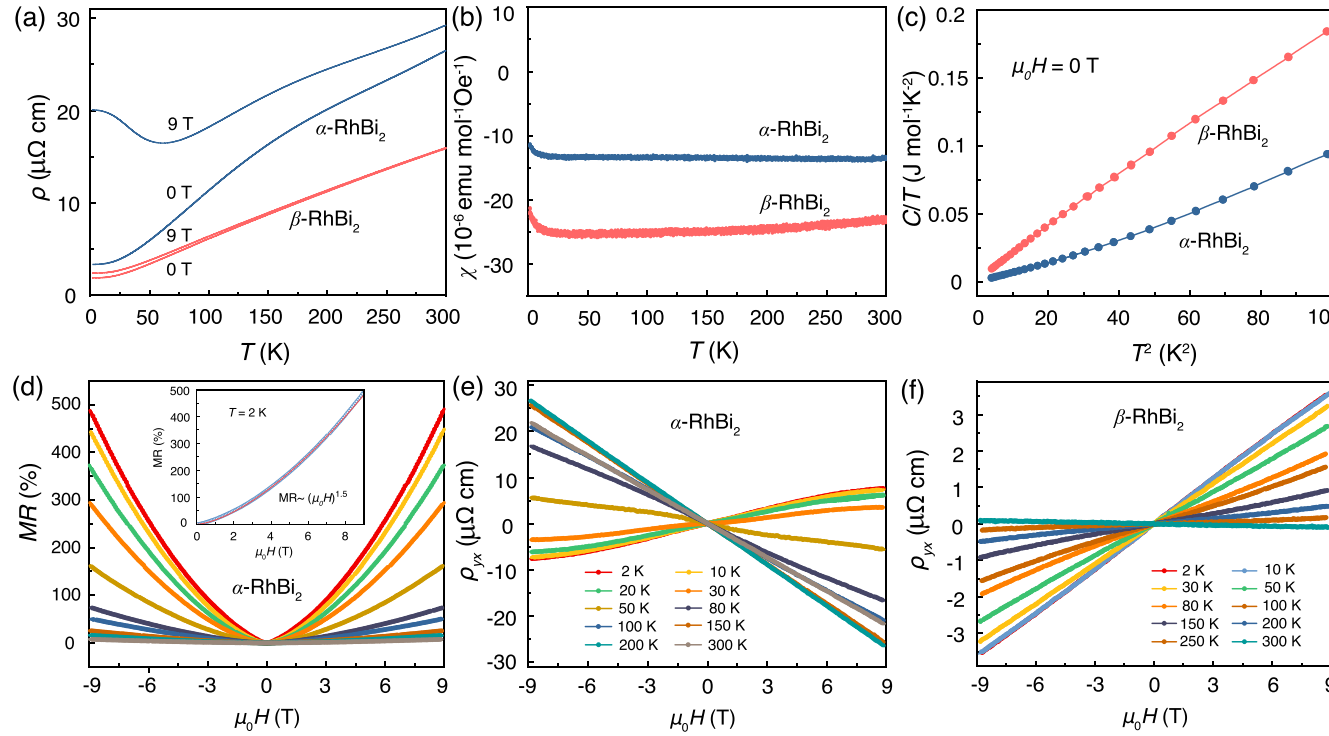


FIG. 3. Physical property measurements of α- and β-$RhBi_2$ at ambient pressure: (a) Temperature dependence of the resistivity without and in a magnetic field of 9 T. (b) Temperature dependence of the magnetic susceptibility measured in a 0.1 T field. (c) Specific heat capacity between 1.8 and 10 K. (d) Magnetoresistance of α-$RhBi_2$ at selected temperatures [legend identical to that in (e)]. (e) Hall resistivity of α-$RhBi_2$ at selected temperatures. (f) Hall resistivity of β-$RhBi_2$ at different temperatures.

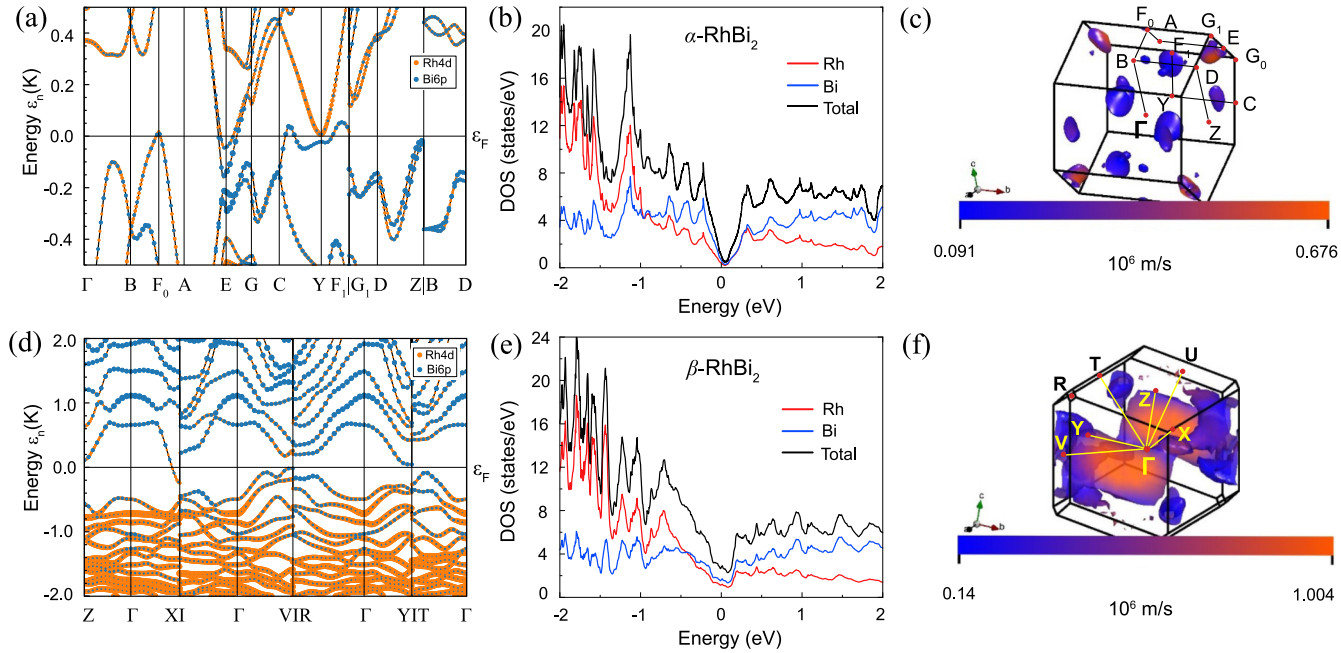


FIG. 4. Electronic structure of $RhBi_2$ polymorphs at ambient pressure. (a) Electronic band structure, (b) total and partial electronic DOS, (c) Fermi surface of α-$RhBi_2$. (d) Electronic band structure, (e) total and partial electronic DOS, and (f) Fermi surface of β-$RhBi_2$.

diamagnetic response is due to a small density of states at the Fermi energy, resulting in a larger core diamagnetic component [27]. The weak upturns observed below 30 K are attributed to dilute paramagnetic impurities or defect moments in the samples.

The measured specific heat capacity $C_p(T)$ is shown in Fig. 3(c). An analysis fitting $C_p = \gamma T + \beta T^3$ with an electronic (with γ being the Sommerfeld coefficient) and a phononic contribution within the Debye approximation in the 1.8–5 K temperature range yields $\gamma = 0.28$ mJ mol^{-1} K^{-2} and $\beta = 0.7$ mJ mol^{-1} K^{-4} for α-$RhBi_2$ and $\gamma = 1.8$ mJ mol^{-1} K^{-2}, $\beta = 2.0$ mJ mol^{-1} K^{-4} for β-$RhBi_2$ (see Fig. S3 [30]). The calculated Debye temperatures $\Theta_D = (\frac{12\pi^4}{5\beta} nR)^{\frac{1}{3}}$ (where n is the number of atoms, and R the molar gas constant) are 203 and 143 K for the α- and β modifications, respectively. The higher Θ_D of α-$RhBi_2$ apparently reflects stronger bonding in the three-dimensional (3D) structure as compared with the somewhat 2D structure of the β-phase with weak interactions between layers. The electronic density of states (DOS) at E_F calculated from γ within the free electron model for β-$RhBi_2$ is 0.76 states eV^{-1}. Such a small but finite value characterizes this polymorph as a metal with nonoverlapping pockets [27]. The very small value of the Sommerfeld coefficient γ of α-$RhBi_2$ may be due to defects and indicates an almost negligible DOS at E_F, implying the semimetal character of the α phase.

These conclusions are corroborated by electronic structure calculations (Fig. 4). According to the band structure analysis and calculated partial electronic densities of states at ambient pressure, the valence bands in both the α [Figs. 4(a) and 4(c)] and β phases [Figs. 4(d) and 4(e)] comprise comparable contributions from Rh 4d states and Bi 6p orbitals. The calculated total DOS for α-$RhBi_2$ demonstrates a pronounced dip around E_F, with negligible DOS at the Fermi level [Fig. 4(b)], whereas the Fermi surface consists of multiple nonoverlapping small electron and hole pockets [Fig. 4(c)], characterizing the α phase as a semimetal. By contrast, the electronic structure for β-$RhBi_2$ [Fig. 4(d)] has a finite DOS at E_F [Fig. 4(e)] and a Fermi surface with multiple electron and hole pockets [Fig. 4(f)], confirming that this polymorph is a metal with nonoverlapping pockets.

The electrical transport of the $RhBi_2$ polymorphs in magnetic fields is also characteristic. Applying a field of 9 T, $\rho(T)$ of β-$RhBi_2$ only exhibits a slight increase at low temperatures [Fig. 3(a)], in agreement with previous studies [27]. However, the resistivity of α-$RhBi_2$ strongly increases with field and even qualitatively changes its temperature dependence below $T \approx 60$ K [Fig. 3(a)]. For α-$RhBi_2$, the magnetoresistance $\mathrm{MR(B)} = [\rho(B) - \rho(0)]/\rho(0)$ reaches a remarkably high value of 500% for 9 T at 2 K [Fig. 3(d)] and shows anomalous behavior, with MR(B) proportional to $B^{1.5}$ [inset in Fig. 3(d)] instead of the conventional quadratic dependence. Such a pronounced positive MR with anomalous dependence on B was observed in some type-II Weyl semimetals, e.g., $TaIrTe_4$ [46] and $NbIrTe_4$ [47,48]. In addition, it was inferred that the proximity to the Weyl points is important for the magnetotransport properties [46]. The $\mathrm{MR(B)} \sim B^{1.5}$ behavior might be attributed to the admixture of the Dirac-like linear magnetoresistance and conventional quadratic magnetoresistance due to the conventional bands. However, this cannot be unambiguously concluded from our experimental data because the latter contribution should saturate at sufficiently high fields (beyond the highest field in our experiment). In a classical picture, the large transverse MR is explainable owing to the proximity to a perfect balance between electron and hole carriers [49]. Indeed, the Hall resistivity of α-$RhBi_2$ varies nonlinearly for $T < 50$ K [Fig. 3(e)], indicating that both electrons and holes contribute to the electrical transport

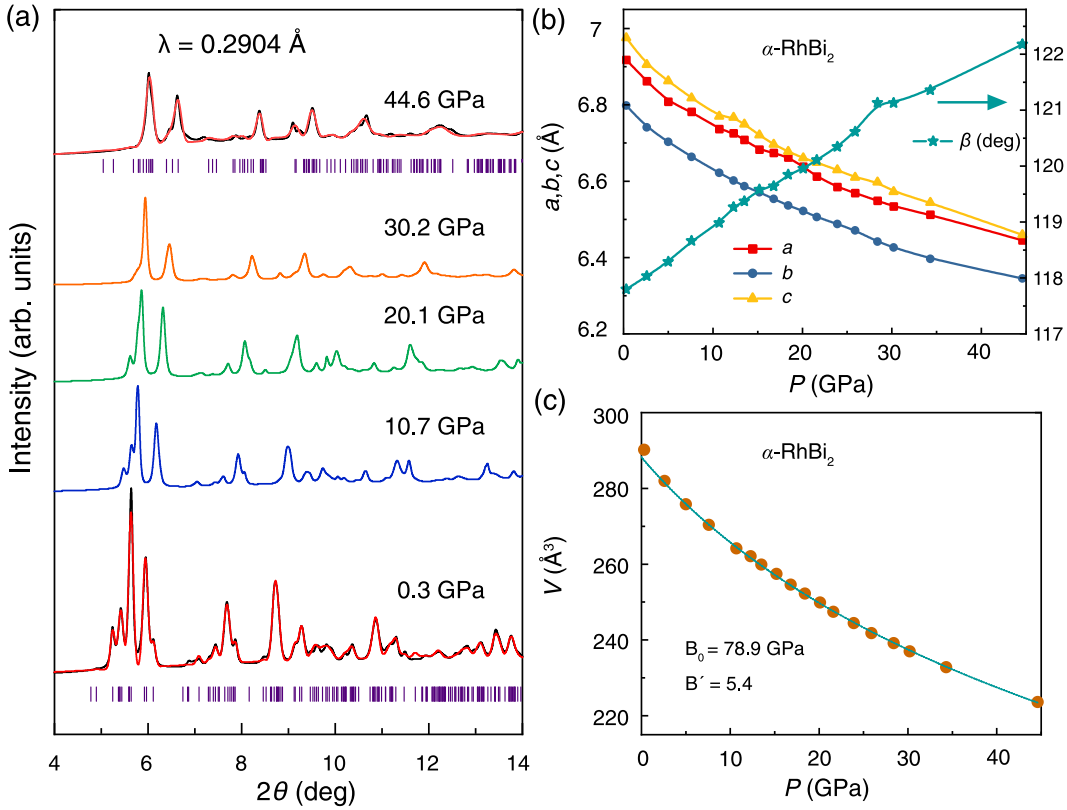


FIG. 5. Pressure effect on the crystal structure of α-$RhBi_2$. (a) Powder XRD patterns at selected pressures. The red lines at 0.3 and 44.6 GPa are the Le Bail fits of the experimental patterns (black line) with a monoclinic structure. (b) Pressure dependence of the refined lattice parameters. (c) Pressure dependence of the unit cell volume. The solid line is the fit of the BM3-EoS to the experimental data.

properties. Fitting the experimental MR data at 2 K with a two-band model yields close values for the electron and hole carrier concentrations, $n_e = 2.1 \times 10^{20}$ cm^{-3} and $n_h = 3.3 \times 10^{20}$ cm^{-3}, respectively (Fig. S4 [30,50]). By contrast, β-$RhBi_2$ shows only a small MR, as evidenced by the nearly identical 0 T and 9 T resistivity curves in Fig. 3(a). In addition, its Hall resistivity is linear with a positive slope [Fig. 3(f)], indicating dominant hole carriers.

B. High-pressure investigations

1. α-$RhBi_2$

Synchrotron PXRD measurements were performed up to 44.6 GPa to investigate the effect of pressure on the crystal structure of α-$RhBi_2$ [Fig. 5(a)]. The PXRD pattern at the lowest experimental pressure of 0.3 GPa can unambiguously be assigned to the $P2_1/c$ monoclinic structure [Fig. 5(a)] with lattice parameters [Fig. 5(b)] in good agreement with the ambient pressure data. As the pressure increases, the patterns show progressive changes [peak broadening, a decrease in the number of observable reflections, see Fig. 5(a)]. However, no new reflections evolve, and even at 44.6 GPa, the PXRD pattern can be satisfactorily modeled within $P2_1/c$ [Fig. 5(a)]. The deduced lattice parameters [Fig. 5(b)] and unit cell volume [Fig. 5(c)] change smoothly with increasing pressure. The changes in PXRD patterns can thus be attributed to pressure-induced broadening of the reflections and their intensity redistribution due to the preferred orientation, which is typical for high-pressure conditions. Any major structural phase transition can be ruled out in the studied pressure range.

The stability of the $P2_1/c$ crystal lattice of α-$RhBi_2$ is supported by phonon spectrum calculations of this monoclinic structure at different pressures up to 40 GPa (Fig. S5 [30]). No imaginary phonon modes are revealed, indicating that the α-$RhBi_2$ structure is dynamically stable within the studied pressure range. The phonon band structure calculations show a progressive hardening of the acoustic modes with increasing compression levels, which also indicates the structural stability of the compound over the full pressure range. Such pressure stability of the distorted marcasite-type structure of α-$RhBi_2$ agrees with the typically wide pressure range of stability of the marcasite structure (such as that demonstrated in Ref. [51]). The fit of the third-order Birch–Murnaghan equation of state (BM3-EoS) [52] to the experimental data of the unit cell volume [Fig. 5(c)] yields a bulk modulus $B_0 = 78.9 \pm 1.8$ GPa and its pressure derivative $B' = 5.4 \pm 0.1$.

The effect of pressure on the electronic transport properties of α-$RhBi_2$ was investigated at applied quasi-hydrostatic pressures up to 40 GPa (Fig. 6). At pressures up to ~20 GPa, the resistivity decreases upon cooling at all pressures, indicating that α-$RhBi_2$ exhibits a normal metallic behavior. No evidence of superconductivity is observed upon cooling to 1.8 K in this pressure range. Notably, elemental bismuth becomes superconducting at temperatures below 4–8 K in the 2.6–10.5 GPa pressure range [53]. The absence of a superconducting transition in our resistivity data at low pressures reveals the

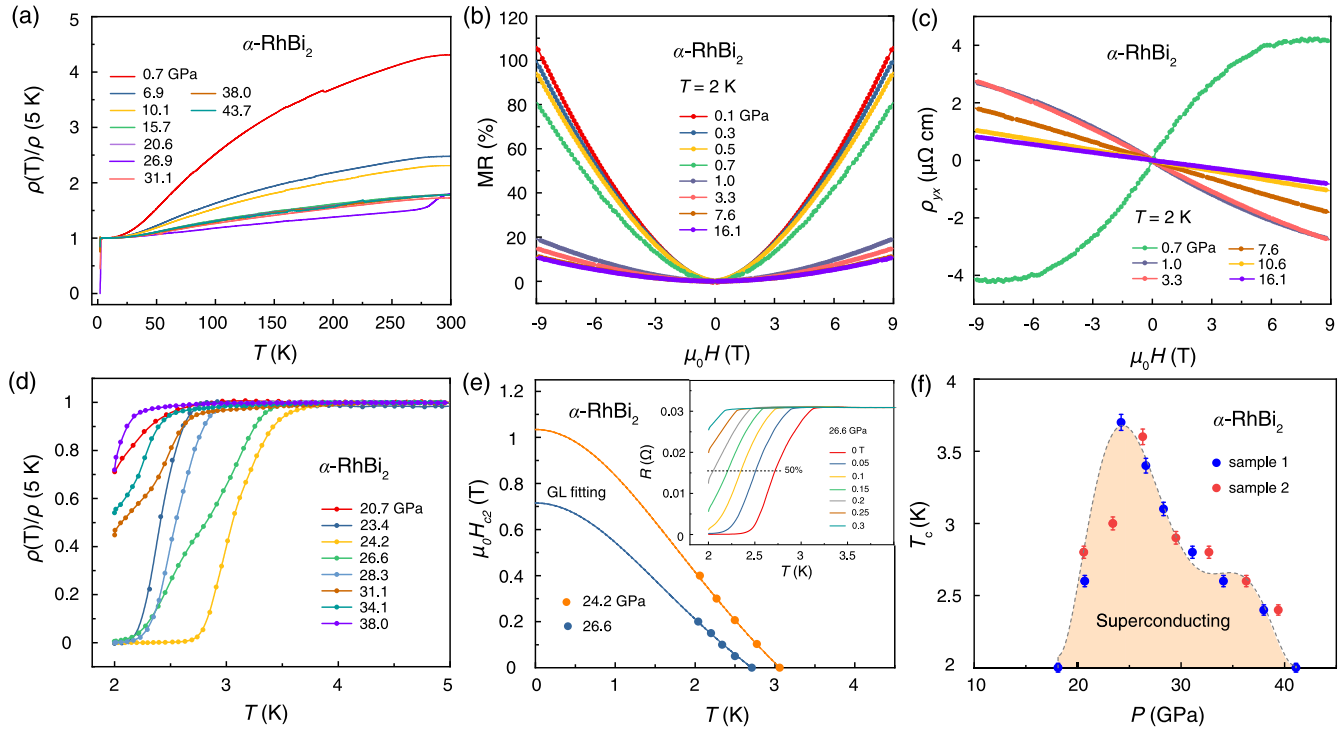


FIG. 6. Pressure-induced superconductivity in α-$RhBi_2$. (a) Normalized temperature dependence of sample resistance at different pressures. (b) Magnetoresistance and (c) Hall resistivity at different pressures at 2 K. (d) Normalized sample resistance below 5 K at different pressures. (e) Temperature dependence of the upper critical field of the superconducting phase at different pressures. Lines represent a fit with the GL model. The inset shows the superconducting transition in the resistivity under different magnetic fields at 26.6 GPa. (f) Pressure dependence of T_c for two different samples. The dashed line is a guide for the eye.

absence of the Bi impurities on the surface of the sample under study.

Application of pressure has a strong effect on the magnetoresistance (MR) of α-$RhBi_2$ [Fig. 6(b) and 6(c)]. MR is rapidly suppressed under pressure and reaches MR(9 T) = 10% at 3.3 GPa [Fig. 6(b)]. At this pressure, the Hall resistivity shows a clear tendency toward linearity and becomes fully linear at pressures above 7.6 GPa with a negative slope, indicating that electrons are the main charge carriers [Fig. 6(c)]. Remarkably, superconductivity emerging along with the suppression of a state with large MR was observed in the type-II Weyl semimetals WTe_2 [54,55] and $NbIrTe_4$ [48]. By contrast, in α-$RhBi_2$, no superconductivity emerges with the suppression of a large MR state; however, the emergence of a superconducting state occurs at a significantly higher pressure.

As the pressure increases up to 20 GPa, an abrupt drop in the resistivity at $T < 2$ K indicates the possible onset of a superconducting transition [Fig. 6(d)]. Zero resistivity can be observed at $p = 23.4$ GPa [Fig. 6(d)], indicating the transition of α-$RhBi_2$ to the superconducting state.

The superconducting state is further confirmed by the evolution of the temperature dependence of the resistivity in an applied magnetic field [see the inset of Fig. 6(e)]. The superconducting transition gradually shifts toward lower temperatures as the magnetic field increases. A fit of the Ginzburg-Landau (GL) relation [56] $\mu_0 H_{c2}(T) = \mu_0 H_{c2}(0)\frac{(1-t^2)}{(1+t^2)}$, where $t = T/T_c$, to the critical field data $H_{c2}(T)$ (Fig. 6(e)) yields the upper critical field values $\mu_0 H_{c2}(0) = 1.03$ and 0.71 T at 24.2 and 26.6 GPa, respectively.

The superconducting transition exhibits a shift toward higher temperatures as the pressure increases to values above 24 GPa. A maximum value of T_c of 3.7 K is reached at $p = 24.2$ GPa. As the pressure increases, T_c decreases gradually to a value of 2 K at the highest pressure in our study (41 GPa), resulting in a dome-shaped dependence of T_c on pressure [Fig. 6(f)].

Thus the pressure-induced superconductivity occurs in the monoclinic α-$RhBi_2$, which is theoretically shown to develop nontrivial topological features in its electronic structure at ambient pressure [28]. The changes in the band structure with pressure are demonstrated in Fig. 7. As the pressure increases, the electronic band structure demonstrates only an observable lowering of the energy in the conduction band in the narrow k region around the E point (Fig. S6 [30]) and profound changes around the Y point [Fig. 7(a)] with a strong hybridization of the Rh 4d and Bi 6p states. Our calculations show a very moderate effect of pressure on the total electronic DOS at E_F [Fig. 7(b)]. However, a look at the pressure-induced modifications of the Fermi surfaces [Fig. 7(c)] reveals the appearance and disappearance of electron and hole pockets. These features suggest the occurrence of multiple Lifshitz transitions, wherein the Fermi surface topology is modified without symmetry breaking, driven purely by changes in external pressure. It thus appears that pressure-induced superconductivity in

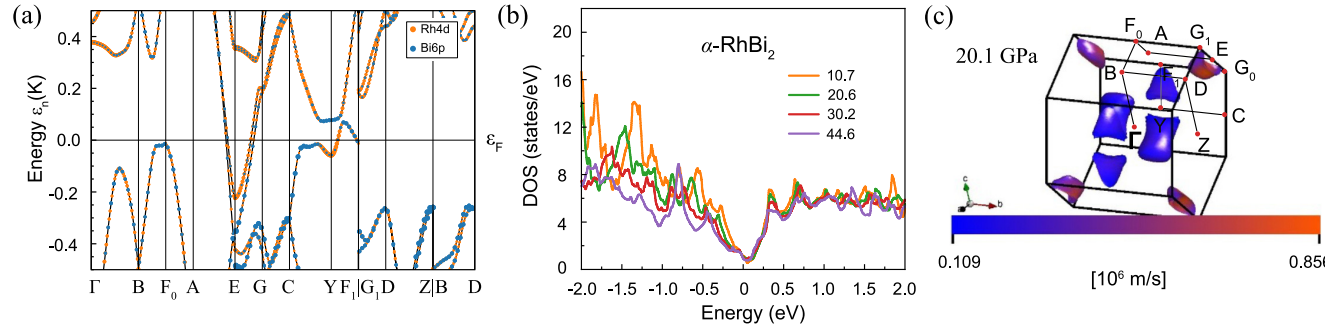


FIG. 7. Pressure effect on electronic structure of α-$RhBi_2$. (a) Electronic band structure at 20.1 GPa, (b) total electronic DOS at different pressures, and (c) Fermi surface at 20.1 GPa.

α-$RhBi_2$ is driven by these changes in the electronic band structure. While the electronic DOS at E_F changes only very slightly with increasing pressure [Fig. 7(b)], calculations of the phonon DOS reveal a shift in the spectral weight toward higher energies under pressure, which appears to cease at $p >$ 30 GPa (Fig. S5 [30]). These changes in the phonon spectrum and the corresponding change in electron-phonon coupling may explain the dome-shaped dependence of T_c on pressure in α-$RhBi_2$.

2. β-$RhBi_2$

The effects of pressure on the crystal structure of β-$RhBi_2$ were investigated via synchrotron SCXRD measurements at pressures up to ∼45 GPa (Fig. 8). The pattern at 0.3 GPa can be attributed to the space group $P\bar{1}$ with refined lattice parameters $a = 6.720$ Å, $b = 7.017$ Å, $c = 7.050$ Å, $\alpha = 104.81°$, $\beta = 100.58°$, and $\gamma = 105.59°$ (Table S2 [30]). These are in good agreement with the ambient pressure data. The diffraction patterns were assigned to the triclinic β-$RhBi_2$ structure up to pressures beyond 12 GPa [Fig. 8(a)].

At pressures above 13 GPa, changes in the diffraction pattern indicate the onset of a structural phase transition (Fig. 8(a)). The high-pressure structure (hereafter referred to as γ-$RhBi_2$) is identified as a tetragonal $CuZr_2$-type structure with space group $I4/mmm$ [Fig. 8(b)]. The refined lattice parameters of this high-pressure phase at 13.5 GPa are

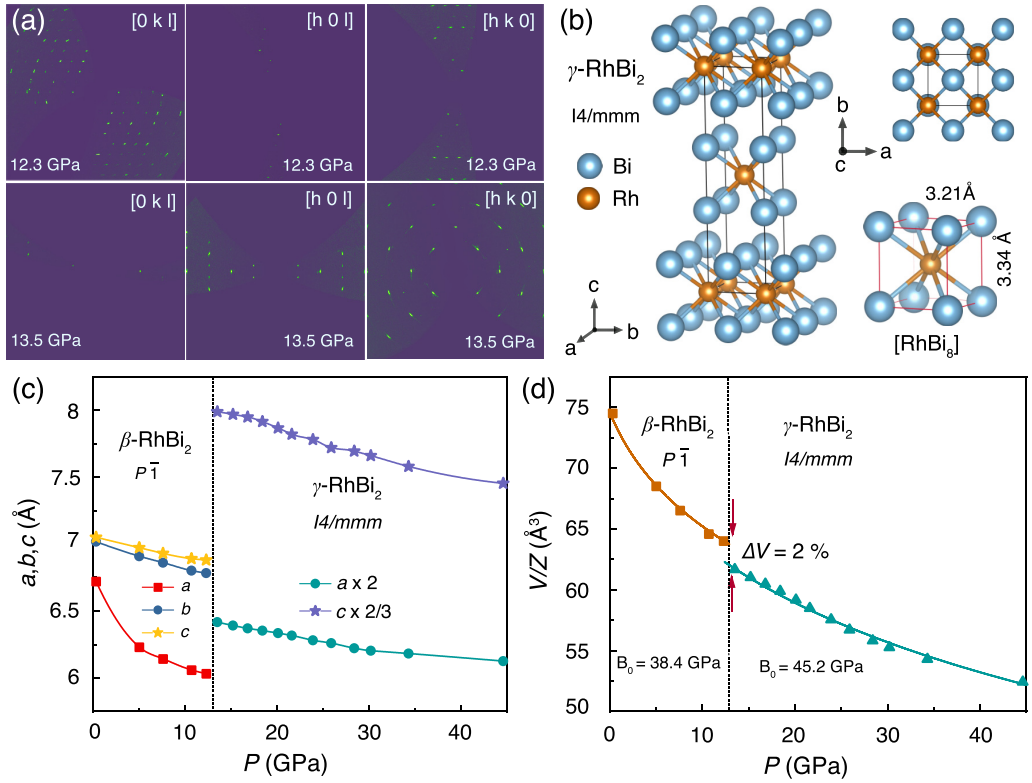


FIG. 8. Crystal structure evolution of β-$RhBi_2$ under applied pressure. (a) Reciprocal space reconstruction in different directions based on single-crystal diffraction demonstrating a pressure-induced structural transition from the triclinic β-$RhBi_2$ (12.3 GPa) to the tetragonal γ-$RhBi_2$ (13.5 GPa) with crystal structure shown in (b). (c) Pressure dependence of lattice parameters. (d) Pressure dependence of the unit cell volume. The dashed line is the fit of the BM3-EoS to the experimental pressure-volume data.

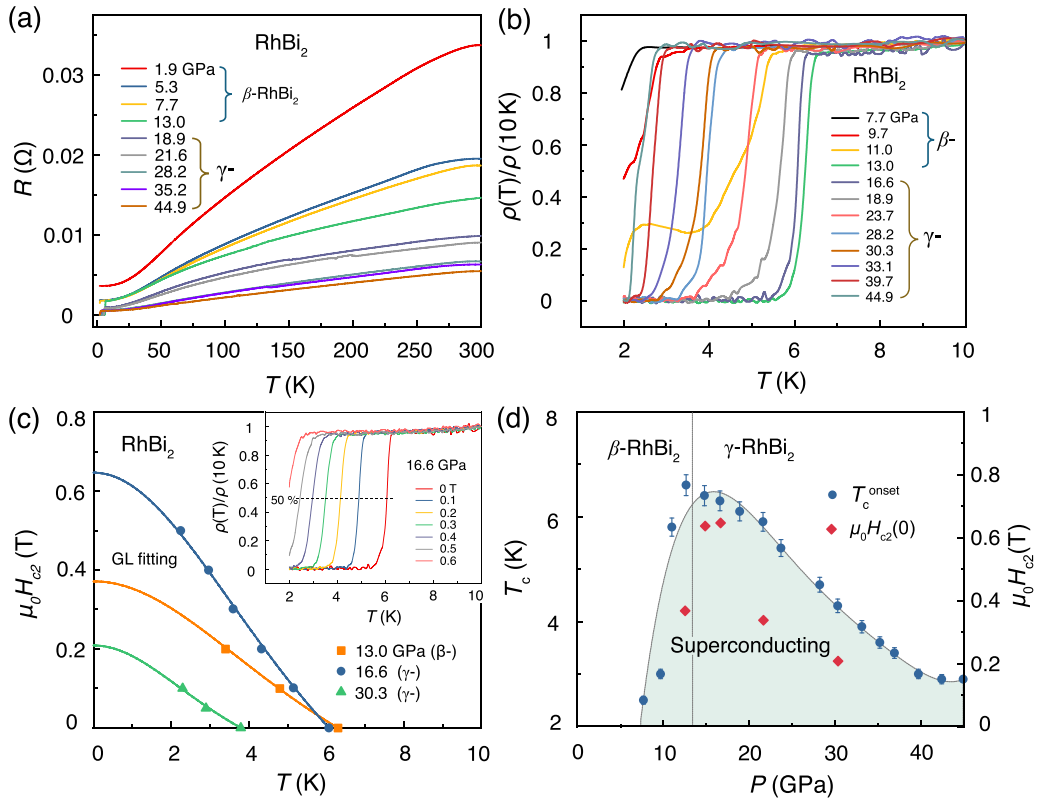


FIG. 9. Pressure-induced superconductivity in β- and γ-$RhBi_2$. (a) Temperature dependence of the sample resistance at different pressures. (b) Normalized resistivity below 10 K displays the superconducting transitions at different pressures. (c) Upper critical field fitting with the GL model at different pressures. The inset shows the superconducting transition in the resistivity under different magnetic fields at 16.6 GPa. (d) Pressure dependence of superconducting transition temperature T_c and extrapolated upper critical field $\mu_0 H_{c2}(0)$. The solid line is a guide for the eye only.

$a = b = 3.208$ Å, and $c = 11.983$ Å [Fig. 8(c)] with Rh atoms in $2a$ (0, 0, 0) and Bi atoms in $4e$ (0, 0, 0.3607) positions (Table S2 [30]). A volume collapse over the structural transition is detected and estimated to be $\Delta V/V \sim 2\%$ [Fig. 8(d)], which is characteristic of a first-order transition. γ-$RhBi_2$ possesses a layered structure formed by layers of eightfold tetragonal prismatically (almost cubically) coordinated Rh atoms [Fig. 8(b)] with a Rh-Bi distance of 2.816 Å. Such a structure is observed in other Rh intermetallic compounds, e.g., $RhTi_2$ [57], and the 3D weak topological insulator $Bi_{14}Rh_3I_9$, which contains layers comprising hexagonal nets of edge-sharing $RhBi_8$ cubes [58]. The tetragonal structure remains stable up to the highest attained pressure of 44.6 GPa [Figs. 8(c) and 8(d)]. Comparing the crystal structures of the low-pressure triclinic β- and high-pressure tetragonal γ modifications, one recognizes that the β-γ structural phase transition only involves a relatively small displacement of atoms (Fig. S7 [30]). Thus the β-γ transition is classified as a displacive structural phase transition.

The temperature dependence of the resistance was measured at different pressures up to ~45 GPa [Fig. 9(a)] to investigate the effect of pressure on the electronic transport properties of β-$RhBi_2$. For pressures up to ~7 GPa, $R(T)$ decreases upon cooling at all pressures, indicating that β-$RhBi_2$ exhibits a normal metallic behavior. As the pressure increases, an abrupt drop in the resistance occurs below 2 K [Fig. 9(b)], indicating the emergence of a superconducting state in β-$RhBi_2$. The transition temperature increases as the pressure approaches the pressure of the structural phase transition to γ-$RhBi_2$ [Figs. 9(b) and 9(d)], and the highest $T_c \approx 6.6$ K is reached at 13 GPa. As the pressure increases further, the superconducting transition temperature begins to decrease.

In the applied magnetic fields, the superconducting transition temperature shifts toward lower values (inset of Fig. 9(c) and Fig. S8 [30]). Fitting the GL equation to the critical field data $\mu_0 H_{c2}(T)$ yields the upper critical field $\mu_0 H_{c2}(0)$ values of 0.37 and 0.65 T at 13.0 and 16.6 GPa, respectively [Figs. 9(c) and 9(d)]. The distinct enhancement of $\mu_0 H_{c2}(0)$ is associated with the structural phase transition to the γ phase above 13 GPa.[1] The obtained values of $\mu_0 H_{c2}(0)$ are significantly below the estimated values within the weak-coupling Bardeen-Schrieffer-Cooper (BCS) theory. Pauli paramagnetic limit ($H_{\text{Pauli}} \approx 1.85[\text{T/K}] \cdot T_c$) [56] values of 11.7, 11.2, and

[1]A significant increase in the upper critical field indicates a structural phase transition at pressures above 13 GPa. Thus the characteristic two-step transition at 11 GPa [Fig. 9(b)] is more likely a measurement artifact than an indication of the coexistence of the β and γ phases. At a pressure of 13 GPa, the sample is in a triclinic β-structure with a single superconducting transition at a temperature corresponding to the higher value of T_c on the curve at 11 GPa.

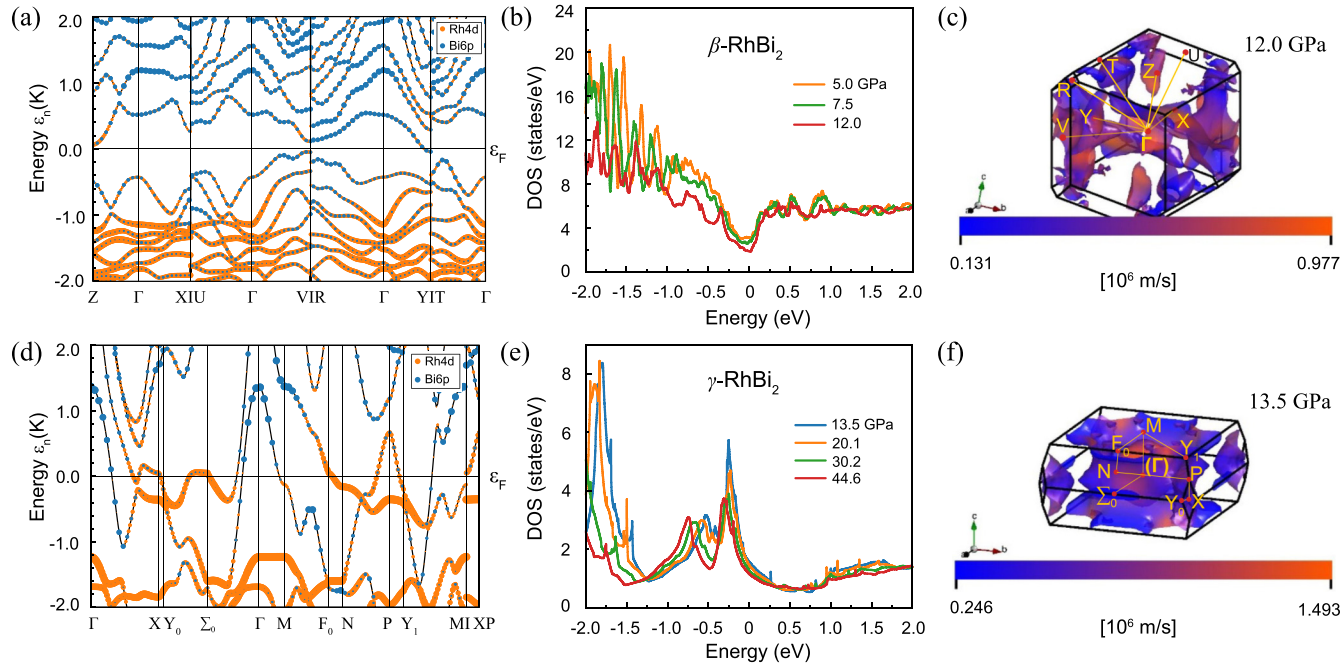


FIG. 10. Electronic structure of β-$RhBi_2$ and γ-$RhBi_2$ at high pressure. (a) Electronic band structure at 12 GPa, (b) total electronic DOS at different pressures, (c) Fermi surface at 12 GPa for β-$RhBi_2$. (d) Electronic band structure at 13.5 GPa, (e) total electronic DOS, and (f) Fermi surface at 13.5 GPa for γ-$RhBi_2$.

7.0 T are calculated for pressures of 13.0, 16.6, and 30.3 GPa, respectively.

The pressure dependences of T_c and $\mu_0 H_{c2}(0)$ are presented in Fig. 9(d). $T_c(p)$ is dome-shaped, with the dome maximum associated with the β-γ structural phase transition. The pressure-induced superconductivity emerges at pressures above 7 GPa within the stability range of the triclinic β phase. The T_c exhibits a rapid increase as pressure increases to 13.0 GPa, with the maximum value of $T_c = 6.6$ K. The distinct enhancement of $\mu_0 H_{c2}(0)$ as the pressure increases [Fig. 9(d)] indicates the transition to the tetragonal γ phase, whereas the T_c in γ-$RhBi_2$ decreased gradually to 2.9 K at the highest attained pressure of 44.9 GPa. Since the pressure-induced superconductivity emerges near the displacive β-γ structural phase transition, we can conclude that the superconductivity in the γ phase is due to a structural instability (soft phonon mode) in the triclinic structure.

The increase in pressure within the stability range of the triclinic structure has only a moderate quantitative effect on the electronic structure of β-$RhBi_2$ [Fig. 10(a)], which remains a metal with low electron DOS at E_F [Fig. 10(b)] and nonoverlapping pockets [Fig. 10(c)]. However, as expected, the structural transition to a tetragonal structure results in significant changes in the electronic band structure [Figs. 10(d)–10(f)]. According to the calculation, the tetragonal γ-$RhBi_2$ is a metal with valence bands predominantly comprising Rh 4d states, whereas the conduction bands primarily originate from Bi 6p orbitals [Fig. 10(d)]. The calculated electronic DOS features a strong peak slightly below the Fermi level [Fig. 10(e)]. The strength of this peak gradually decreases as the pressure increases, leading to a continuous decrease in the T_c with pressure in γ-$RhBi_2$.

The high-pressure phase γ-$RhBi_2$ is isostructural to the superconducting β modification of $PdBi_2$ [21], and this has recently attracted significant interest primarily owing to topologically protected surface states and multiphase superconductivity observations [6,59–63] with possible unconventional pairing [63]. The values of T_c and $\mu_0 H_{c2}(0)$ for γ-$RhBi_2$ (present study) are close to those of β-$PdBi_2$ [64]. In addition, the decrease in T_c with increasing pressure is similar to the pressure evolution of the superconductivity in β-$PdBi_2$ [64]. Furthermore, the Fermi surface of γ-$RhBi_2$ comprises a large central pocket and a network connected along the edges of the Brillouin zone [Fig. 10(f)] and appears to be similar to that of β-$PdBi_2$ [59]. Thus further investigations of the high-pressure phase of $RhBi_2$ are of interest to reveal the interplay between the crystal and electronic structure and unusual electronic properties.

C. Point-contact measurements

Motivated by the possible nontrivial topological electronic properties of α- and β-$RhBi_2$ and the observation of pressure-induced superconductivity, we have performed point-contact (PC) Andreev-reflection spectroscopy [65], which is known to be an effective tool for observing enhanced or tip-induced superconductivity in several topological systems [66–70], even nonsuperconducting ones at ambient pressure.

Figure 11 shows the differential resistance dV/dI curves for PCs at the (a) α-$RhBi_2$ and (b) β-$RhBi_2$ phases, measured with the Cu counterelectrodes. The shape of dV/dI in Figs. 11(a) and 11(b) with a deep zero-bias minimum and symmetrical side maxima is typical for all measured PCs. The zero-bias minimum in dV/dI is connected to the

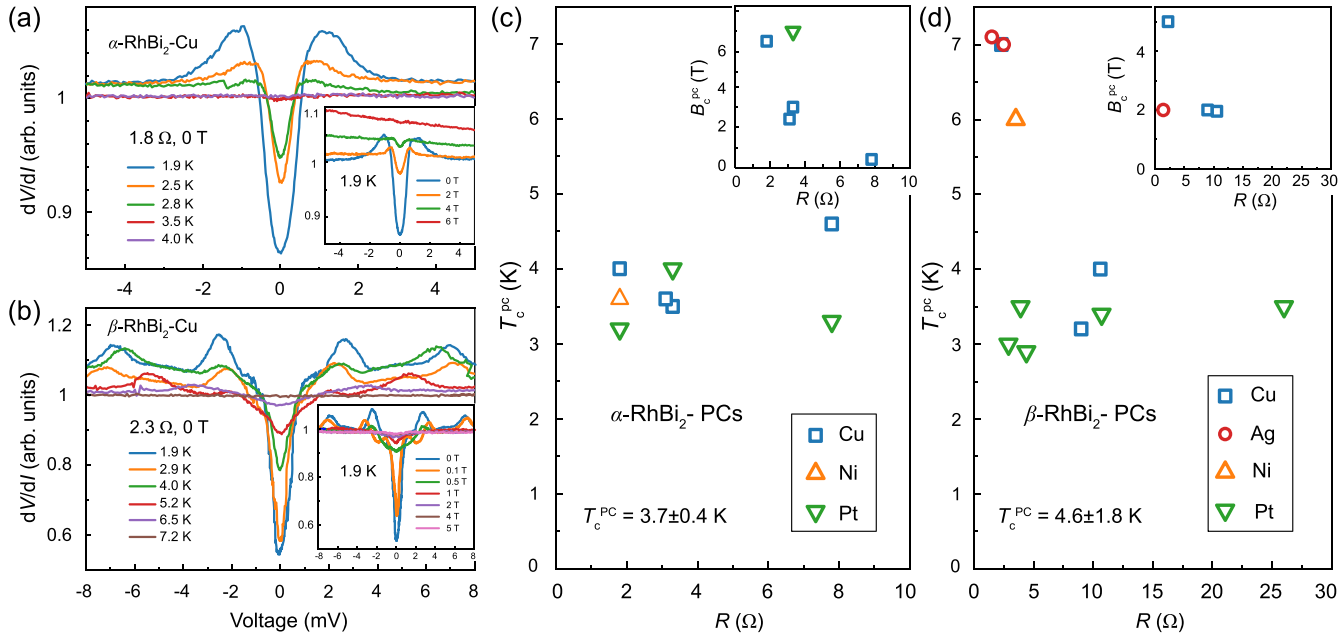


FIG. 11. Temperature variation of the dV/dI of $RhBi_2$ PCs with the highest T_c of (a) approximately 4 K for α-$RhBi_2$ and (b) 7 K for β-$RhBi_2$. The insets show the dV/dI behavior of the PCs in a magnetic field at $T = 1.9$ K. The T_c distribution for all measured heterocontacts with metal (Cu, Ag, Ni, and Pt) counterelectrodes for the (c) α-$RhBi_2$ and (d) β-$RhBi_2$ PCs. Insets: critical magnetic field values for some PCs. The x axis shows PC resistance in the normal state.

superconducting transition because its intensity decreases as the temperature or magnetic field is increased [Figs. 11(a) and 11(b) with insets]. The pronounced side maxima with a zero-bias minimum are characteristic of the nonspectral regime in PCs when the superconducting state is suppressed by a sufficiently high current density, which increases with voltage and results in the heating of the PC core. Therefore these data can only reveal information regarding the critical superconducting temperature and magnetic field values in the PCs.

Figures 11(c) and 11(d) show the distribution of T_c for all measured heterocontacts with elemental metal counterelectrodes (Cu, Ag, Ni, Pt) based on α- and β-$RhBi_2$, respectively. The average T_c for all measured PCs on α-$RhBi_2$ is 3.7 ± 0.4 K, whereas it reaches 4.6 ± 1.8 K for PCs on β-$RhBi_2$. The maximal T_c for α-$RhBi_2$ PCs is ≈ 4.5 K [Fig. 11(c)], which is comparable to the maximum T_c of 3.7 K achieved at pressures above 24 GPa in the bulk. Notably, the PC studies on several materials demonstrated local T_c enhancements (see Ref. [71] and the references therein). This may be owing to the influence of the pressure present at the creation of the PCs. The pressure-related origin of the enhanced T_c in the PCs is supported by the fact that T_c also increases under pressure in the same bulk material. By contrast, pressures exceeding several GPa are likely unachievable in simple pressure-type PCs (see the discussion in Ref. [72]). The PCs on the triclinic β-$RhBi_2$ demonstrated even higher T_c values up to 7 K [Fig. 11(d)], with a rather broad T_c distribution in the measured PCs. Such broad T_c distributions may be affected by the 2D character of the triclinic β-$RhBi_2$ crystal structure. Concurrently, such high T_c values may also be due to the realization of unconventional (topological) surface superconductivity.

PCs with a ferromagnetic tip (Ni) [Figs. 11(c) and 11(d)] also show significantly enhanced T_c values. Thus the enhanced superconductivity in the PCs on $RhBi_2$ is compatible with the ferromagnetism at the tip. The critical magnetic field in the PCs also increases significantly [Figs. 11(c) and 11(d), insets], reaching up to 7 T, similar to the case of the PCs on α-$RhBi_2$.

IV. CONCLUSION

This study provides a comprehensive experimental investigation into the physical properties of the polymorphic phases of the intermetallic compound $RhBi_2$ under ambient- and high-pressure conditions. Characterization of the physical properties revealed that β-$RhBi_2$ is a metal with a low density of states at the Fermi level, in agreement with the findings of previous studies, whereas α-$RhBi_2$ is a semimetal with a large magnetoresistance. Andreev-reflection spectroscopy demonstrates induced superconductivity in the point contacts of normal metals with $RhBi_2$ phases.

Under applied pressure, both $RhBi_2$ phases exhibit pressure-induced superconductivity with a dome-shaped dependence of the T_c on pressure. β-$RhBi_2$ becomes superconducting above 7 GPa and reaches a maximum T_c of 6.6 K at 13 GPa. By comparison, α-$RhBi_2$ exhibits superconductivity at pressures above 20 GPa, with a maximum T_c of 3.7 K at 24.2 GPa. The crystal structure of α-$RhBi_2$ is stable within the entire pressure range investigated up to 45 GPa, whereas β-$RhBi_2$ undergoes a displacive structural phase transition from a triclinic to a tetragonal structure (γ-$RhBi_2$) at 13.5 GPa. γ-$RhBi_2$ is isostructural with β-$PdBi_2$, which has recently attracted considerable attention owing to topologically protected surface states and multiphase superconductivity observations.

The emergence of superconductivity in α-$RhBi_2$ can be explained by electronic instability (Lifshitz transitions) induced by external pressure, whereas the dome-shaped dependence of the T_c on pressure is likely due to changes in the phonon spectrum under pressure. The emergence of superconductivity in β-$RhBi_2$ and the rapid increase in T_c near the displacive β-γ phase transition can be explained by a structural instability (soft mode) in the β phase. The decrease in T_c in the γ phase is attributed to a reduction in the intensity of the peak near the E_F in the electronic density of states.

The combination of topologically nontrivial electronic states, PC- and pressure-induced superconductivity, and the emergence of a new structural phase in the $RhBi_2$ polymorphic system provides interesting insights into the interplay between topologically nontrivial electronic structures, crystal structures, and superconductivity.

ACKNOWLEDGMENTS

This work was supported by the collaboration between the Kavli Foundation, Klaus Tschira Stiftung, and Kevin Wells as part of the SuperC collaboration. The authors acknowledge Deutsche Elektronen Synchrotron (DESY) for granting the beamtime at the P02.2 Extreme Conditions Beamline, the European Synchrotron Radiation Facility (ESRF) for the beamtime provided, and Prof. Andrew Fitch for supervising the experiment at beamline ID22. We are indebted to Yu. G. Naidyuk for helpful comments on point-contact spectroscopy data. O.E.K. acknowledges the grant of the Alexander von Humboldt Foundation (Philipp Schwartz Initiative) and the support of the National Academy of Sciences of Ukraine under project $\Phi 19-5$. T.D. thanks the Collaborative Research Center SFB 1143 (Project ID: 695247310070).

DATA AVAILABILITY

There are no publicly available research data or software supporting this manuscript. Requests for further information or data should be sent to the authors.

[1] A. R. Paul, M. Mukherjee, and D. Singh, A critical review on the properties of intermetallic compounds and their application in the modern manufacturing, Cryst. Res. Technol. **57**, 2100159 (2022).

[2] Q. Gu, G. Krauss, Y. Grin, and W. Steurer, Comparative high-pressure study and chemical bonding analysis of Rh_3Bi_{14} and isostructural $Rh_3Bi_{12}Br_2$, J. Solid State Chem. **180**, 940 (2007).

[3] K. Wang, L. Wang, I.-L. Liu, F. Boschini, M. Zonno, M. Michiardi, E. Rotenberg, A. Bostwick, D. Graf, B. J. Ramshaw, A. Damascelli, and J. Paglione, Symmetry-enforced Fermi degeneracy in topological semimetal $RhSb_3$, Phys. Rev. Mater. **7**, 074205 (2023).

[4] W. Gao, N. Hao, F.-W. Zheng, W. Ning, M. Wu, X. Zhu, G. Zheng, J. Zhang, J. Lu, H. Zhang, C. Xi, J. Yang, H. Du, P. Zhang, Y. Zhang, and M. Tian, Extremely large magnetoresistance in a topological semimetal candidate pyrite $PtBi_2$, Phys. Rev. Lett. **118**, 256601 (2017).

[5] S. Changdar, O. Suvorov, A. Kuibarov, S. Thirupathaiah, G. Shipunov, S. Aswartham, S. Wurmehl, I. Kovalchuk, K. Koepernik, C. Timm, B. Büchner, I. C. Fulga, S. Borisenko, and J. van den Brink, Topological nodal *I*-wave superconductivity in $PtBi_2$, Nature (London) **647**, 613 (2025).

[6] K. Iwaya, Y. Kohsaka, K. Okawa, T. Machida, M. Bahramy, T. Hanaguri, and T. Sasagawa, Full-gap superconductivity in spin-polarised surface states of topological semimetal β-$PdBi_2$, Nat. Commun. **8**, 976 (2017).

[7] Y. S. Hor, A. J. Williams, J. G. Checkelsky, P. Roushan, J. Seo, Q. Xu, H. W. Zandbergen, A. Yazdani, N. P. Ong, and R. J. Cava, Superconductivity in $Cu_xBi_2Se_3$ and its implications for pairing in the undoped topological insulator, Phys. Rev. Lett. **104**, 057001 (2010).

[8] Shruti, V. K. Maurya, P. Neha, P. Srivastava, and S. Patnaik, Superconductivity by Sr intercalation in the layered topological insulator Bi_2Se_3, Phys. Rev. B **92**, 020506(R) (2015).

[9] T. Asaba, B. J. Lawson, C. Tinsman, L. Chen, P. Corbae, G. Li, Y. Qiu, Y. S. Hor, L. Fu, and L. Li, Rotational symmetry breaking in a trigonal superconductor Nb-doped Bi_2Se_3, Phys. Rev. X **7**, 011009 (2017).

[10] J. L. Zhang, S. J. Zhang, H. M. Weng, W. Zhang, L. X. Yang, Q. Q. Liu, S. M. Feng, X. C. Wang, R. C. Yu, L. Z. Cao, L. Wang, W. G. Yang, H. Z. Liu, W. Y. Zhao, S. C. Zhang, X. Dai, Z. Fang, and C. Q. Jin, Pressure-induced superconductivity in topological parent compound Bi_2Te_3, Proc. Natl. Acad. Sci. USA **108**, 24 (2011).

[11] K. Kirshenbaum, P. S. Syers, A. P. Hope, N. P. Butch, J. R. Jeffries, S. T. Weir, J. J. Hamlin, M. B. Maple, Y. K. Vohra, and J. Paglione, Pressure-induced unconventional superconducting phase in the topological insulator Bi_2Se_3, Phys. Rev. Lett. **111**, 087001 (2013).

[12] M. Sato and Y. Ando, Topological superconductors: A review, Rep. Prog. Phys. **80**, 076501 (2017).

[13] S. Ono, H. C. Po, and H. Watanabe, Refined symmetry indicators for topological superconductors in all space groups, Sci. Adv. **6**, eaaz8367 (2020).

[14] N. P. Butch, P. Syers, K. Kirshenbaum, A. P. Hope, and J. Paglione, Superconductivity in the topological semimetal YPtBi, Phys. Rev. B **84**, 220504(R) (2011).

[15] Z. K. Liu, L. X. Yang, S.-C. Wu, C. Shekhar, J. Jiang, H. F. Yang, Y. Zhang, S.-K. Mo, Z. Hussain, B. Yan, C. Felser, and Y. L. Chen, Observation of unusual topological surface states in half-Heusler compounds LnPtBi (Ln = Lu, Y), Nat. Commun. **7**, 12924 (2016).

[16] F. Tafti, T. Fujii, A. Juneau-Fecteau, S. René de Cotret, N. Doiron-Leyraud, A. Asamitsu, and L. Taillefer, Superconductivity in the noncentrosymmetric half-Heusler compound LuPtBi: A candidate for topological superconductivity, Phys. Rev. B **87**, 184504 (2013).

[17] G. Xu, W. Wang, X. Zhang, Y. Du, E. Liu, S. Wang, G. Wu, Z. Liu, and X. X. Zhang, Weak antilocalization effect and

noncentrosymmetric superconductivity in a topologically nontrivial semimetal LuPdBi, Sci. Rep. **4**, 5709 (2014).

[18] O. Pavlosiuk, D. Kaczorowski, X. Fabreges, A. Gukasov, and P. Wiśniewski, Antiferromagnetism and superconductivity in the half-Heusler semimetal HoPdBi, Sci. Rep. **6**, 18797 (2016).

[19] H. Kim, K. Wang, Y. Nakajima, R. Hu, S. Ziemak, P. Syers, L. Wang, H. Hodovanets, J. D. Denlinger, P. M. R. Brydon, D. F. Agterberg, M. A. Tanatar, R. Prozorov, and J. Paglione, Beyond triplet: Unconventional superconductivity in a spin-3/2 topological semimetal, Sci. Adv. **4**, eaao4513 (2018).

[20] E. J. Rode, Izvest. Inst. Platiny Drug. Blagorodn. Met. **7**, 21 (1929).

[21] N. Zhuravlev and G. Zhdanov, An X-ray investigation of compounds in the systems Bi-Rh and Bi-Pd in relation to superconductivity studies, Izv. Akad. Nauk SSSR, Ser. Fiz. **20**, 708 (1956).

[22] F. Weitzer, W. Schnelle, R. C. Gil, S. Hoffmann, R. Giedigkeit, and Y. Grin, Phase relationship and superconductivity in the Bi-rich part of the binary system Rh–Bi, Calphad **33**, 27 (2009).

[23] P. Kainzbauer, K. W. Richter, and H. Ipser, The binary Bi-Rh phase diagram: Stable and metastable phases, J. Phase Equilib. Diffus. **39**, 17 (2018).

[24] X. Zhang, H. Lei, and C. Petrovic, Superconducting state in the metastable binary bismuthide Rh_3Bi_{14} single crystals, Phys. Rev. B **86**, 054502 (2012).

[25] M. Ruck, Kristallstruktur und Zwillingsbildung der intermetallischen phase β-Bi_2Rh, Acta Crystallogr. Sect. B **52**, 605 (1996).

[26] E. L. Muetterties and C. M. Wright, Molecular polyhedra of high co-ordination number, Q. Rev. Chem. Soc. **21**, 109 (1967).

[27] K. Lee, G. F. Lange, L.-L. Wang, B. Kuthanazhi, T. V. Trevisan, N. H. Jo, B. Schrunk, P. P. Orth, R.-J. Slager, P. C. Canfield, and A. Kaminski, Discovery of a weak topological insulating state and van Hove singularity in triclinic $RhBi_2$, Nat. Commun. **12**, 1855 (2021).

[28] X. Yang and Y. Li, Topological properties and strain effects of binary monoclinic superconductors RhX_2 (X = Sb,Bi), Physica B **650**, 414569 (2023).

[29] H.-K. Mao, X.-J. Chen, Y. Ding, B. Li, and L. Wang, Solids, liquids, and gases under high pressure, Rev. Mod. Phys. **90**, 015007 (2018).

[30] See Supplemental Material at http://link.aps.org/supplemental/10.1103/8bx1-db7f for pressure-induced superconductivity in the $RhBi_2$ polymorphs.

[31] A. Fitch, C. Dejoie, E. Covacci, G. Confalonieri, O. Grendal, L. Claustre, P. Guillou, J. Kieffer, W. de Nolf, S. Petitdemange, M. Ruat, and Y. Watier, ID22 – The high-resolution powder-diffraction beamline at ESRF, J. Synchrotron Radiat. **30**, 1003 (2023).

[32] L. Akselrud and Y. Grin, *WinCSD*: Software package for crystallographic calculations (version 4), J. Appl. Crystallogr **47**, 803 (2014).

[33] H.-P. Liermann, Z. Konôpková, W. Morgenroth, K. Glazyrin, J. Bednarčik, E. E. McBride, S. Petitgirard, J. T. Delitz, M. Wendt, Y. Bican, A. Ehnes, I. Schwark, A. Rothkirch, M. Tischer, J. Heuer, H. Schulte-Schrepping, T. Kracht, and H. Franz, The extreme conditions beamline P02.2 and the Extreme conditions science infrastructure at PETRA III, J. Synchrotron Radiat. **22**, 908 (2015).

[34] C. Prescher and V. B. Prakapenka, *DIOPTAS*: A program for reduction of two-dimensional X-ray diffraction data and data exploration, High Press. Res. **35**, 223 (2015).

[35] B. H. Toby and R. B. Von Dreele, *GSAS-II*: The genesis of a modern open-source all purpose crystallography software package, J. Appl. Crystallogr. **46**, 544 (2013).

[36] R. O. Diffraction, CrysAlisPro software system, Version 1.171.43.105a, Rigaku Corporation, Wroclaw, Poland (2021).

[37] G. M. Sheldrick, *SHELXT* – Integrated space-group and crystal-structure determination, Acta Crystallogr. A **71**, 3 (2015).

[38] G. Sheldrick, Crystal structure refinement with SHELXL, Acta Crystallogr. C **71**, 3 (2015).

[39] O. Dolomanov, L. Bourhis, R. Gildea, J. Howard, and H. Puschmann, *OLEX2*: A complete structure solution, refinement and analysis program, J. Appl. Crystallogr. **42**, 339 (2009).

[40] K. Momma and F. Izumi, *VESTA3* for three-dimensional visualization of crystal, volumetric and morphology data, J. Appl. Crystallogr. **44**, 1272 (2011).

[41] K. Koepernik, Full potential local orbital minimum basis band-structure scheme, https://www.fplo.de/.

[42] K. Koepernik and H. Eschrig, Full-potential nonorthogonal local-orbital minimum-basis band-structure scheme, Phys. Rev. B **59**, 1743 (1999).

[43] A. Togo and I. Tanaka, First principles phonon calculations in materials science, Scr. Mater. **108**, 1 (2015).

[44] G. Kresse and J. Furthmüller, Efficient iterative schemes for *ab initio* total-energy calculations using a plane-wave basis set, Phys. Rev. B **54**, 11169 (1996).

[45] A. Kjekshus, B. Nolander, P. Klaeboe, S. Cyvin, I. Lagerlund, and L. Ehrenberg, On the properties of binary compounds with the $CoSb_2$ type crystal structure, Acta Chem. Scand. **25**, 411 (1971).

[46] E. Haubold, K. Koepernik, D. Efremov, S. Khim, A. Fedorov, Y. Kushnirenko, J. van den Brink, S. Wurmehl, B. Büchner, T. K. Kim, M. Hoesch, K. Sumida, K. Taguchi, T. Yoshikawa, A. Kimura, T. Okuda, and S. V. Borisenko, Experimental realization of type-II Weyl state in noncentrosymmetric $TaIrTe_4$, Phys. Rev. B **95**, 241108(R) (2017).

[47] X.-W. Huang, X.-X. Liu, P. Yu, P.-L. Li, J. Cui, J. Yi, J.-B. Deng, J. Fan, Z.-Q. Ji, F.-M. Qu, X.-N. Jing, C.-L. Yang, L. Lu, Z. Liu, and G.-T. Liu, Magneto-transport and Shubnikov–de Haas oscillations in the type–II Weyl semimetal candidate $NbIrTe_4$ flake*, Chin. Phys. Lett. **36**, 077101 (2019).

[48] Q.-G. Mu, F.-R. Fan, H. Borrmann, W. Schnelle, Y. Sun, C. Felser, and S. Medvedev, Pressure-induced superconductivity and modification of Fermi surface in type-II Weyl semimetal $NbIrTe_4$, npj Quantum Mater. **6**, 55 (2021).

[49] M. N. Ali, J. Xiong, S. Flynn, J. Tao, Q. D. Gibson, L. M. Schoop, T. Liang, N. Haldolaarachchige, M. Hirschberger, N. P. Ong, and R. J. Cava, Large, non-saturating magnetoresistance in WTe_2, Nature (London) **514**, 205 (2014).

[50] J. M. Ziman, *Electrons and Phonons: Theory of Transport Phenomena in Solids* (Clarendon Press, Oxford, 1962).

[51] K. Niwa, T. Terabe, K. Suzuki, Y. Shirako, and M. Hasegawa, High-pressure stability and ambient metastability of marcasite-type rhodium pernitride, J. Appl. Phys. **119**, 065901 (2016).

[52] T. Katsura and Y. Tange, A simple derivation of the Birch–Murnaghan equations of state (EOSs) and comparison with EOSs derived from other definitions of finite strain, Minerals **9**, 745 (2019).

[53] Y. Li, E. Wang, X. Zhu, and H.-H. Wen, Pressure-induced superconductivity in Bi single crystals, Phys. Rev. B **95**, 024510 (2017).

[54] D. Kang, Y. Zhou, W. Yi, C. Yang, J. Guo, Y. Shi, S. Zhang, Z. Wang, C. Zhang, S. Jiang, A. Li, K. Yang, Q. Wu, G. Zhang, L. Sun, and Z. Zhao, Superconductivity emerging from a suppressed large magnetoresistant state in tungsten ditelluride, Nat. Commun. **6**, 7804 (2015).

[55] X.-C. Pan, X. Chen, H. Liu, Y. Feng, Z. Wei, Y. Zhou, Z. Chi, L. Pi, F. Yen, F. Song, X. Wan, Z. Yang, B. Wang, G. Wang, and Y. Zhang, Pressure-driven dome-shaped superconductivity and electronic structural evolution in tungsten ditelluride, Nat. Commun. **6**, 7805 (2015).

[56] M. Tinkham, *Introduction to Superconductivity* (Courier Corporation, Mineola, NY, 2004).

[57] R. Kuentzler and R. Waterstrat, Electronic properties, superconductivity and stability of the ordered alloys of the Ti-Rh, Zr-Rh and Hf-Rh isoelectronic systems, Solid State Commun. **68**, 85 (1988).

[58] B. Rasche, A. Isaeva, M. Ruck, S. Borisenko, V. Zabolotnyy, B. Büchner, K. Koepernik, C. Ortix, M. Richter, and J. van den Brink, Stacked topological insulator built from bismuth-based graphene sheet analogues, Nat. Mater. **12**, 422 (2013).

[59] M. Sakano, K. Okawa, M. Kanou, H. Sanjo, T. Okuda, T. Sasagawa, and K. Ishizaka, Topologically protected surface states in a centrosymmetric superconductor β-$PdBi_2$, Nat. Commun. **6**, 8595 (2015).

[60] P. K. Biswas, D. G. Mazzone, R. Sibille, E. Pomjakushina, K. Conder, H. Luetkens, C. Baines, J. L. Gavilano, M. Kenzelmann, A. Amato, and E. Morenzoni, Fully gapped superconductivity in the topological superconductor β-$PdBi_2$, Phys. Rev. B **93**, 220504 (2016).

[61] L. Che, T. Le, C. Q. Xu, X. Z. Xing, Z. Shi, X. Xu, and X. Lu, Absence of Andreev bound states in β-$PdBi_2$ probed by point-contact Andreev reflection spectroscopy, Phys. Rev. B **94**, 024519 (2016).

[62] J. Kačmarčík, Z. Pribulová, T. Samuely, P. Szabó, V. Cambel, J. Šoltýs, E. Herrera, H. Suderow, A. Correa-Orellana, D. Prabhakaran, and P. Samuely, Single-gap superconductivity in β-Bi_2Pd, Phys. Rev. B **93**, 144502 (2016).

[63] L. Powell, W. Kuang, G. Hawkins-Pottier, R. Jalil, J. Birkbeck, Z. Jiang, M. Kim, Y. Zou, S. Komrakova, S. Haigh, I. Timokhin, G. Balakrishnan, A. K. Geim, N. Walet, A. Principi, and I. V. Grigorieva, Multiphase superconductivity in $PdBi_2$, Nat. Commun. **16**, 291 (2025).

[64] G. Pristáš, M. Orendáč, S. Gabáni, J. Kačmarčík, E. Gažo, Z. Pribulová, A. Correa-Orellana, E. Herrera, H. Suderow, and P. Samuely, Pressure effect on the superconducting and the normal state of β-Bi_2Pd, Phys. Rev. B **97**, 134505 (2018).

[65] Y. G. Naidyuk and K. Gloos, Anatomy of point-contact Andreev reflection spectroscopy from the experimental point of view, Low Temp. Phys. **44**, 257 (2018).

[66] H. Wang, H. Wang, H. Liu, H. Lu, W. Yang, S. Jia, X.-J. Liu, X. Xie, J. Wei, and J. Wang, Observation of superconductivity induced by a point contact on 3D Dirac semimetal Cd_3As_2 crystals, Nat. Mater. **15**, 38 (2016).

[67] H. Wang, H. Wang, Y. Chen, J. Luo, Z. Yuan, J. Liu, Y. Wang, S. Jia, X.-J. Liu, J. Wei, and J. Wang, Discovery of tip induced unconventional superconductivity on Weyl semimetal, Sci. Bull. **62**, 425 (2017).

[68] H. Wang, Y. He, Y. Liu, Z. Yuan, S. Jia, L. Ma, X.-J. Liu, and J. Wang, Ferromagnetic tip induced unconventional superconductivity in Weyl semimetal, Sci. Bull. **65**, 21 (2020).

[69] H. Wang, L. Ma, and J. Wang, Tip-induced or enhanced superconductivity: A way to detect topological superconductivity, Sci. Bull. **63**, 1141 (2018).

[70] S. Howlader and G. Sheet, Tip-induced superconductivity, J. Phys.: Condens. Matter **33**, 403002 (2021).

[71] D. Bashlakov, O. Kvitnitskaya, G. Shipunov, S. Aswartham, O. Feya, D. Efremov, B. Büchner, and Y. G. Naidyuk, Electron-phonon interaction and point contact enhanced superconductivity in trigonal $PtBi_2$, Low Temp. Phys. **48**, 747 (2022).

[72] Y. G. Naidyuk, G. Fuchs, D. A. Chareev, and A. N. Vasiliev, Doubling of the critical temperature of FeSe observed in point contacts, Phys. Rev. B **93**, 144515 (2016).